Research Project

Using physical modelling to examine
the urban heat island effect in Sydney

Author	S. Lamey
Student #	47768583
Course	GEOM7001
Words	6081

Contents

Introduction

Urban areas trap and radiate heat in ways that profoundly alter how people live and work. The Urban Heat Island (UHI) effect describes the relative warmth of urban areas compared to rural surroundings, driven by urban topology, heat-absorbing materials, reduced green space, and anthropogenic heat emissions (Christen et al., 2017). Understanding the diurnal dynamics of UHI is critical to managing public health and environmental sustainability in urban environments. Traditionally, UHI monitoring relied on sparse ground stations. Remote sensing now provides a transformative alternative, enabling continuous spatiotemporal measurements of land surface temperature (LST) that are impossible with ground stations alone (Muller et al., 2013).

Research Problem

The central question of this project is how heat flux in Syndney varies across space and time, from day to night. Nighttime investigations are particularly important, as UHI is typically strongest at night. Without solar irradiance, urban materials with high thermal inertia (e.g concrete, bitumen) retain heat, while rural areas cool more quickly through radiative loss (Christen et al., 2017; Oke, 1982). Dense built environments also create an 'urban canyon' effect, trapping and reradiating heat between vertical surfaces.

However, two challenges hinder remote sensing of UHI and must be reckoned with. Firstly, city-scale studies, which are concerned with the more ephemeral dynamics of heat flux, demand both fine spatial detail and high temporal frequency. However, satellite platforms typically trade off one for the other. Secondly, analysis-ready nighttime satellite scenes are relatively scarce (Mao et al., 2021). Landsat-8/9 ascending passes, for example, only acquire nocturnal thermal data from the TIRS sensor. The optical OLI sensor does not collect yet both are needed for thermal correction. As a result, USGS only releases Level-1 nocturnal scenes, without atmospheric correction, LST or surface reflectance subdata (Zanter, 2016).

Physical modelling plays a central role in deriving LSTs and thereby enabling an assessment of the UHI effect. By modelling surface emissivity, atmospheric

attenuation, and radiative transfer, these approaches provide physically consistent LST estimates at the native resolution of the satellite sensor (Yu et al., 2014). This makes physical modelling well suited to applications where high spatial detail is needed, such as resolving contrasts across an urban landscape.

In this study, physical modelling techniques are used to generate daytime and nighttime LSTs for Sydney. They then form the basis for UHI analysis. It is important to note, however, that these modelling steps serve primarily as a means of deriving reliable thermal inputs rather than constituting the focus of the research. The core aim of this paper is to investigate the patterns, drivers, and spatial structure of UHI in Sydney, rather than to evaluate or advance LST modelling methods, as reflected in the research aims outlined below.

Research Aims

Primary Objective

1. "To analyse the diurnal variations in Sydney's UHI during the summer heatwave from November 2019 - January 2020".

Secondary Objective

2. "To derive high-resolution daytime and nighttime LSTs for use in UHI via physical modelling"

Study Area and Study Period

The study area is within the Greater Sydney metropolitan region, as shown in Figure 1. To define the area, a bounding box was extracted from the bounds of the Greater Sydney area as per the Australian Bureau of Statistic's (ABS) Statistical Areas Level-4. Table 1 summarises the geometry of the study area in WGS84:

Table 1: Geometry of the study area in Sydney

Parameter	Value
X_min, Y_min	150.301560°E, -34.316218°S
X_max, Y_max	151.477327°E, -33.403931°S
Width	122.01 km

Height	116.58 km
Area	11009.36 km^2

Sydney has a dense urban core which shows strong UHI effects with built-up areas in its central business district (CBD) frequently 4 to 10 °C hotter than surrounding suburbs. Streetscapes are the most heat-sensitive elements, usually about 1 to 4 °C hotter than rooftops. Urban greenery plays an important role in cooling Sydney's microclimate through evapotranspiration and shading. Suburbs with higher urban greenery ratios, such as the Harbour, tended to be 1.6 °C cooler than the CBD average, representing a statistically significant difference (Sharifi & Lehmann, 2014).
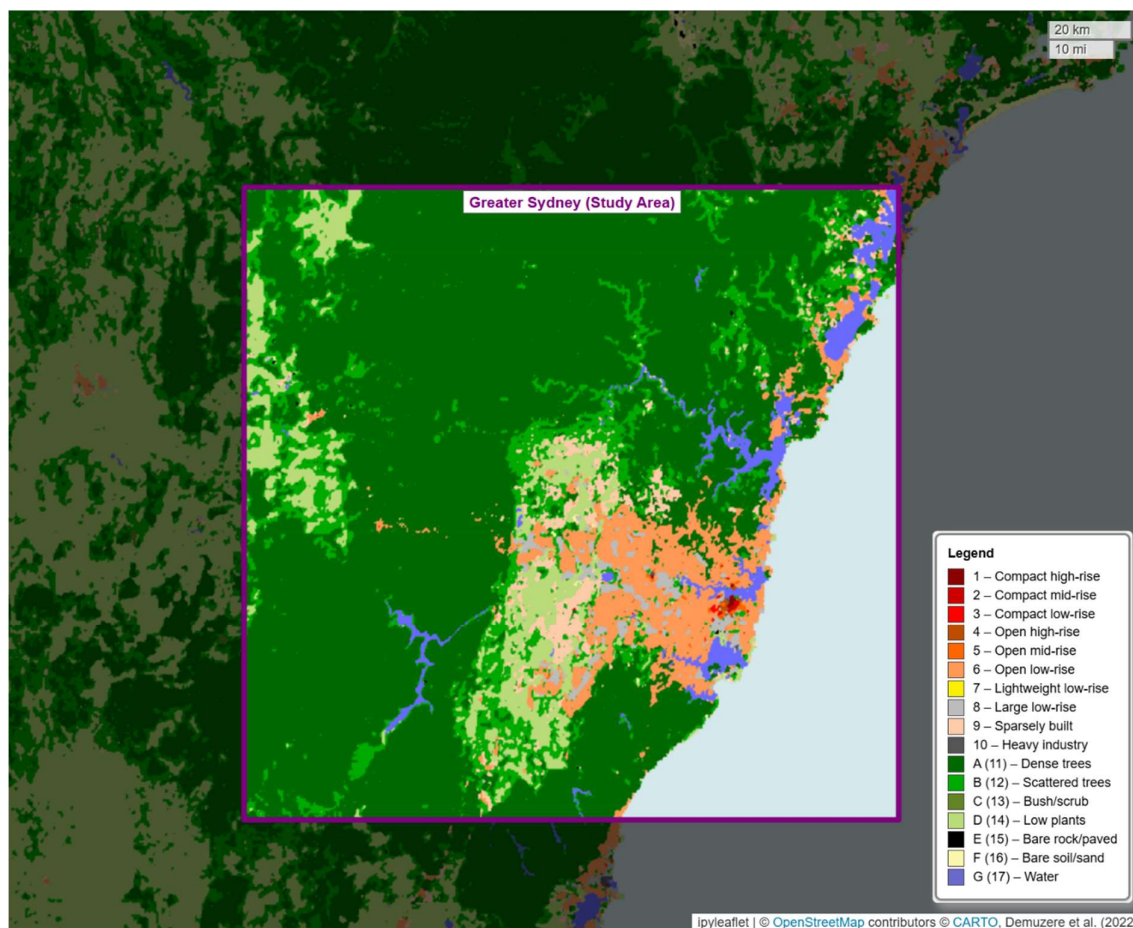

Figure 1: The study area of the Greater Sydney metropolitan region

The intensity of Sydney's UHI varies temporally. Daytime heating in eastern suburbs is sometimes offset by sea breezes, while slow nighttime heat release from built materials prolongs high inland temperatures. Sydney's subtropical climate further shapes the seasonality of UHI. During the summer months, Sydney's LSTs tend to reach higher absolute magnitudes, but the diurnal contrast between day and night is less pronounced due to high background temperatures and persistent heat storage. In contrast, winter UHIs are weaker overall but display greater diurnal variability (Sharifi & Lehmann, 2014). These climatic conditions impose important constraints on satellite-based UHI assessments. Summer generally maximises LST magnitudes, but it is also characterised by higher rates of cloud cover, rainfall, and wind, resulting in less atmospheric stability and stronger advective heat transfer (Yun et al., 2020).

A distinct opportunity emerged for this study, however. Sydney's $2019 - 2020$ summer coincided with an extreme, persistent heatwave, producing high temperature anomalies. Critically, heatwaves are typically marked by strong synoptic stability (Oliveira et al., 2022). Thus, this summer period aligned with multiple clear-sky Landsat nighttime overpasses. Such a rare overlap provides a highly favourable natural experiment for examining UHI dynamics using thermal remote sensing.

Literature Review

The relationship between radiance, temperature and wavelength is the basis of thermal remote sensing. Every object with a temperature above absolute zero (i.e 0 K) emits radiation. Planck's law describes the amount of radiation emitted by a blackbody at wavelength λ and temperature T:

$$B_\lambda(T) = \frac{2hc^2}{\lambda^5 \left[\exp\left(\frac{hc}{\lambda T}\right) - 1 \right]} \qquad [1].$$

Where $B_\lambda(T)$ is the spectral radiance $[Wm^{-2}\mu m^{-1}sr^{-1}]$ of a blackbody at temperature T $[K]$ and wavelength λ $[\mu m]$; c is the speed of light at 2.9979e8 $[ms^{-1}]$; h is the Planck constant at 6.6261e-34 $[Js]$; and k is the Boltzmann constant at 1.3806e-23 $[JK^{-1}]$.

Since most real-world surfaces are not perfect blackbodies, radiance calculations must account for their emissivity ε, which expresses how efficiently the surface emits thermal radiation relative to an ideal blackbody. Additionally, top-of-atmosphere (TOA) radiance describes the radiance received by the sensor at a given wavelength. However, retrieving LST is more complex than simply inverting Planck's law on this value. The received signal includes not only surface radiation but also atmospheric contributions. Thus, surface emission, along with atmospheric upwelling and downwelling radiance, must all be accounted for (Li et al., 2013). A simplified radiative transfer equation can express the apparent radiance received by the sensor along its line-of-sight:

$$B_i(T_i) = \tau_i(\theta)[\varepsilon_i B_i(T_s) + (1 - \varepsilon_i)L^d_i] + L^u_i \qquad [2].$$

Where $B_i(T_i)$ is the radiance received by band i with a brightness temperature of T_i $[K]$; τ_i is the atmospheric transmittance, corrected for the viewing zenith angle θ of the sensor; ε_i is the surface emissivity; and L^d_i and L^u_i are downwelling and upwelling path radiances $[Wm^{-2}\mu m^{-1}sr^{-1}]$.

Thus, through Planck's inversion, surface temperature can be solved:

$$T_s = \frac{2hc^2}{\lambda_i \ln\left(\dfrac{hc}{\lambda_i^5(B_i(T_i) - L^u_i - \tau_i(1 - \varepsilon_i)L^d_i)/\tau_i \varepsilon_i} + 1\right)} \qquad [3].$$

Where λ_i is the effective wavelength for band i, which is defined according to its spectral response function (i.e its sensitivity to different wavelengths across the electromagnetic spectrum) (Yu et al., 2014).

Retrieving LST from daytime and nighttime Landsat 8 scenes requires several sequential steps. First, TOA radiance, TOA reflectance, and brightness temperature must be computed from the raw digital numbers (DNs). Next, surface emissivity is estimated from surface reflectance products. With emissivity established, the necessary atmospheric parameters can be modelled and applied to derive LST (Oliveira et al., 2022). These LST maps form the basis for UHI estimation, calculated by subtracting a rural reference temperature from each pixel (Jia et al., 2024).

Datasets

Landsat

Landsat-8/9 provide data from 2013 until present achieving a combined revisit time of 8 days (or 16 days singularly). Across the OLI and TIRS instruments, 11 spectral bands are provided: 8 in the visible (VIS), near-infrared (NIR), and shortwave infrared (SWIR) at 30m resolution, a 15m panchromatic band, and 2 thermal infrared (TIR) bands at 100m (Zanter, 2016).

While nighttime TIRS scenes provide the thermal information used for LST retrieval, corresponding daytime acquisitions enable estimations of emissivity through surface reflectance. A key constraint is that the USGS provides nighttime TIRS data only at Level-1, which lacks OLI acquisitions. To ensure methodological consistency between daytime and nighttime processing, all Landsat imagery used in this study is therefore sourced at Level-1. Data are taken from Collection 2, with higher-quality Tier-1 scenes selected wherever possible. The Landsat datasets incorporated in this study include:

Table 2: Landsat datasets used

Name	Level	Product ID	Spatial Resolution	Temporal Resolution
Landsat-8/9 Nighttime TIRS	L1	LT08_L1TP LT09_L1TP	30m	Not-fixed; opportunistic
Landsat-8/9 Daytime OLI/TIRS	L1	LC08_L1TP LC08_ L1TP	30m	8-days

ERA5 Reanalysis Data

To model the atmospheric contributions required for LST retrieval, this study incorporates ERA5, the fifth-generation global reanalysis produced by the European Centre for Medium-Range Weather Forecasts (ECMWF). ERA5 provides hourly atmospheric and surface variables from 1940 to present at a spatial resolution of 0.25° (C3S, 2018).

Of particular relevance to thermal remote sensing, ERA5 supplies vertical profiles up to 30km with estimations of specific humidity, temperature, and pressure. These

variables enable estimation of precipitable water vapour and gas number densities, which thereby enable the simulation of atmospheric transmittance and upwelling/downwelling radiance components (Mayer et al., 2025). Because Landsat nighttime scenes lack Level-2 atmospheric correction products, ERA5 provides the necessary atmospheric information for both daytime and nighttime LST retrieval.

Table 3: ERA5 datasets used

Name	Level	Product ID	Spatial Resolution
ERA5 Reanalysis	n/a	doi.org/10.24381/cds.adbb2d47	0.25° (resampled to 30m)

Auxiliary Datasets

To estimate and analyse UHI intensity (UHII), a rural reference baseline is required. This study uses the ABS Urban Centres and Localities (UCL) dataset, a vector product that delineates urban and rural areas at approximately the Statistical Area Level 1 (Australian Bureau of Statistics, 2021). After classifying each pixel as urban or rural, the rural mean LST can be derived, enabling the conversion of LSTs to UHI intensity (Jia et al., 2024).

Because this analysis also seeks to examine how land cover and urban form influence UHII patterns, Local Climate Zones (LCZs) are incorporated using the Global LCZ Map at 100 m resolution (resampled to 30 m). While coarser than some other products, such as Digital Earth Australia's Landcover, the Global LCZ Map offers a unique advantage in classification of urban morphology types (e.g. open low-rise, compact high-rise, heavy industry, etc.). These classes directly correspond to the structural and functional characteristics of the urban environment that influence LST and UHI. Thus, the Global LCZ Map provides a meaningful representation of urban form (Demuzere et al., 2022).

Table 4: Auxiliary datasets used

Name	Level	Product ID	Spatial Resolution
Urban Centres and Localities	n/a	1270.0.55.004	n/a
LCZ Global Map	n/a	doi.org/10.5281/zenodo.6364593.	100m (resampled to 30m)

Validation Dataset

No in-situ LST measurements were available within the study area for the period examined. As a result, direct ground-based validation of the retrieved LSTs was not possible. Instead, model outputs were assessed against the official Landsat Collection 2 Level-2 LST product provided by the USGS. Because this product is derived directly from the underlying Level-1 acquisitions, it shares the same spatiotemporal characteristics, namely a 30 m spatial resolution (resampled from 100 m TIRS data) and an effective 8-day revisit cycle when Landsat-8 and Landsat-9 are combined (Zanter, 2016).

Table 5: Validation datasets used

Name	Level	Product ID	Spatial Resolution
Landsat-8/9 LST	L2	LC08_L2SP / LC09_L2SP	n/a

Methods

A python installation was used for the full processing workflow (see Chart 1). Only the thermal infrared bands from TIRS are available for Landsat 8 nighttime acquisitions. Consequently, the USGS does not generate surface temperature products for night scenes because the visible and near infrared bands, typically required for emissivity estimation, are absent. As a result, the TIRS data must be manually processed into an analysis-ready form. Applying a consistent processing workflow across both day and night scenes is key for ensuring LST estimates remain comparable.
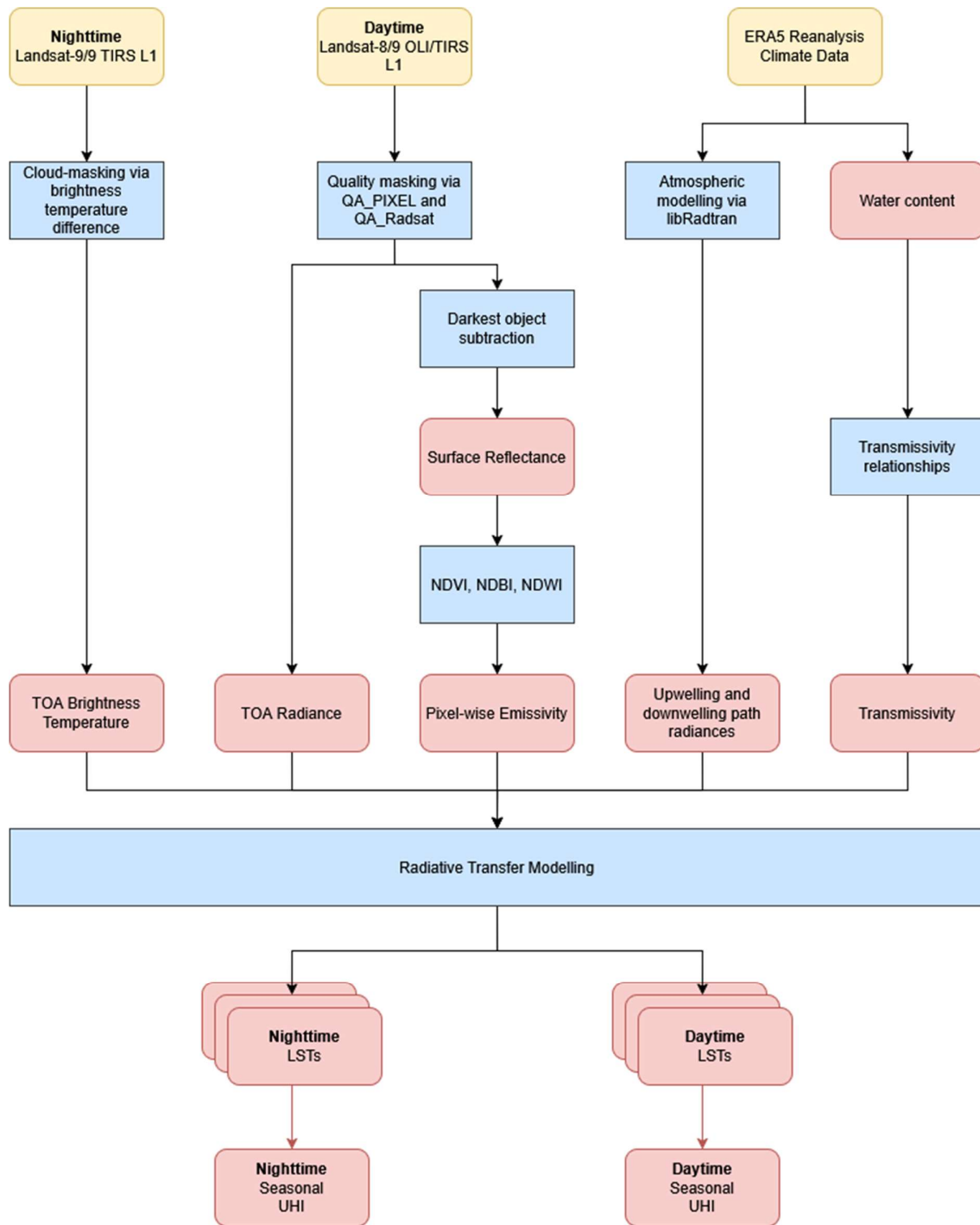
Chart 1: The processing workflow

Data Selection and Quality Masking

Nighttime acquisitions are comparatively rare and are not consistently available across online data platforms. Therefore, a manual search was conducted using

USGS' *EarthExplorer* to identify clear-sky scenes with a maximum cloud cover of 10%. This filter remains unset for nighttime scenes. As a result, all candidate nighttime scenes required manual inspection for cloud contamination and surface conditions. This search process yielded 11 clear-sky daytime scenes and 5 nighttime scenes.

Following retrieval, both the daytime and nighttime scenes were masked for quality control. Landsat 8 Level-1 products provide two per-scene quality assurance layers, QA_PIXEL and QA_RADSAT, each encoding pixel-level conditions using single- and double-bit flags. QA_PIXEL identifies pixels affected by conditions such as no-data, cloud, cloud shadow, water, and provides associated confidence levels. QA_RADSAT flags pixels compromised by radiometric saturation or terrain occlusion (Zanter, 2016). For daytime scenes, these two layers were used to generate a clear-pixel mask by excluding all pixels flagged as cloud, snow, water, shadow, terrain-occluded, or radiometrically saturated, requiring low confidence for these conditions.

Because the generation of QA layers relies on the combined use of OLI and TIRS observations, these layers are empty for nighttime scenes. Consequently, cloud masking for night scenes was performed manually. Clouds are typically much colder than land surfaces at night, and the spectral signatures of cloud types remain broadly similar across visible to shortwave-infrared wavelengths but diverge markedly in the thermal infrared. Leveraging these properties, clouds were identified and masked through thresholds applied to (i) absolute brightness temperature and (ii) the brightness-temperature difference between bands 10 and 11 (Candra et al., 2019).

Preprocessing

Converting Landsat digital numbers (DN) to top-of-atmosphere (TOA) radiance, TOA reflectance, and brightness temperature follows the standard procedures outlined in the Landsat 8 Data User's Guide (Zanter, 2016). Each of these quantities is derived using the appropriate radiometric rescaling coefficients provided in the scene metadata, as shown in equations $[4] - [6]$.

$$\lambda_i = A_i + M_i\, Q_i \qquad\qquad [4].$$

Where λ_i is the TOA radiance for band i; Q_i is the DN of the Level-1 pixel; M_i is the radiance multiplicative scaling factor in the scene metadata; and A_i is the radiance additive scaling factor in the scene metadata.

TOA reflectance is similarly derived:

$$\rho_i = A_i + M_i Q_i \qquad [5].$$

Where ρ_i is the TOA reflectance for band i; Q_i is the DN of the Level-1 pixel; M_i is the reflectance multiplicative scaling factor in the scene metadata; and A_i is the reflectance additive scaling factor in the scene metadata.

Finally, brightness temperature can be derived as a product of TOA radiance:

$$T_i = \frac{K_1}{\ln\left(\frac{K_2}{\lambda_i} + 1\right)} \qquad [6].$$

Where T_i is the brightness temperature for band i; and K_1 and K_2 are constants available in the scene metadata.

Surface Reflectance

Subsequently, surface reflectance for the OLI bands was derived from TOA reflectance using the darkest object subtraction (DOS) method (J. Chavez Pat, 1996). DOS offers a simple and computationally efficient means of reducing atmospheric scattering effects and normalising reflectance values across scenes acquired under varying illumination and atmospheric conditions, as expressed in equation [7]:

$$\rho_s = \rho_{TOA} - \rho_{haze} \qquad [7].$$

Where ρ_s is surface reflectance; ρ_{TOA} is TOA reflectance; ρ_{haze} is the reflectance value of the darkest object(s) in a scene.

Valid dark objects typically include terrain slopes in full shadow and, in some cases, deep water; however, sedimented water should be avoided because it exhibits elevated reflectance in red and green bands. Procedurally, the haze reflectance term ρ_{haze} can be estimated using either the absolute minimum pixel value or a low percentile ($< 1\%$) of the reflectance distribution (P. S. Chavez, 2014). This study employed the latter approach and constrained corrected reflectance values to above zero.

Emissivity

Surface indices are essential inputs for estimating surface emissivity. This study employed the NDVI-based emissivity algorithm developed by Sobrino et al. (2008). Because the original formulation was designed for rural environments, the modifications proposed by Wicki and Parlow (2017) to better account for urban conditions were incorporated. Accordingly, two additional indices were calculated: the Normalised Difference Built-up Index (NDBI) and the Normalised Difference Water Index (NDWI). All three indices are defined in equations $[8] - [10]$:

$$NDVI = \frac{NIR - RED}{NIR + RED} \qquad [8.]$$

$$NDBI = \frac{SWIR_1 - NIR}{SWIR_1 + NIR} \qquad [9.]$$

$$NDBI = \frac{GREEN - NIR}{GREEN + NIR} \qquad [10.]$$

Pixels dominated by vegetation $NDVI > 0.5$ ($NDVI_v$) were assigned an emissivity of 0.99 (ε_v). Water bodies, identified by $NDVI \geq 0.0$ were set to an emissivity of 0.98. Bare-soil pixels $NDVI < 0.2$ ($NDVI_s$) were mapped to an emissivity of 0.97 (ε_s). Built-up areas were identified using with $NDBI > -0.2$ in combination with $NDVI \leq 0.35$. These urban areas were assigned an emissivity of 0.9612 based on mean emissivity of construction materials (i.e brick, concrete, etc.). Finally leftover pixels were those with $0.2 \leq NDVI \leq 0.5$, whose emissivity (ε_i) was determined according to equation [11]:

$$\varepsilon_i = \varepsilon_v P_v + \varepsilon_s(1 - P_v) + C \qquad\qquad [11.]$$

Where P_v, the vegetation portion of pixel i, is a function of the pixel's NDVI value, the vegetation threshold ($NDVI_v$), and the bare-soil threshold ($NDVI_s$):

$$P_v = \left(\frac{NDVI_i - NDVI_s}{NDVI_v - NDVI_s}\right)^2 \qquad\qquad [12].$$

And C is the cavity effect:

$$C = \varepsilon_v(1 - \varepsilon_s)F'(1 - P_v) \qquad\qquad [13].$$

Where F' is a dimensionless geometrical factor typically derived from the combination of OLI and TIRS observations (Wicki & Parlow, 2017). However, following Sobrino et al (2004), a mean value of 0.55 was adopted because optical data were not available for all scenes. A pixel-wise emissivity map was generated for each daytime scene across the study period, and these maps were subsequently mosaicked and composited by taking the median value in areas of overlap (see Figure 1 in *Results*).

Atmospheric Parameters

Downwelling (L^d) and Upwelling (L^u) Path Radiances

To solve the radiative transfer equation for LST, the atmospheric components—upwelling and downwelling path radiance— must be estimated. These parameters can be modelled using *libRadtran*, which simulates radiative transfer from vertical atmospheric profiles describing the atmospheric state at discrete pressure levels. The software requires, at minimum, six key variables: geopotential height $[km]$, pressure $[mb]$, temperature $[K]$, dry-air number density $[cm^{-3}]$, water-vapour number density $[cm^{-3}]$, and ozone number density $[cm^{-3}]$ (Mayer et al., 2025).

ERA5 provides these parameters through an hourly global reanalysis at 0.25° (~30km) spatial resolution, extending to approximately 30 km altitude (C3S, 2018).

Above this height, atmospheric density becomes sufficiently low that absorption and scattering of thermal infrared radiation contribute minimally to the radiative transfer process. For each Landsat scene, the nearest-hour ERA 5 profile was selected via nearest neighbour. These profiles were downloaded and supplied to *libRadtran* to simulate the atmospheric radiance components, namely L^u and L^d. To isolate L^d from surface-emitted contributions, the surface temperature and surface albedo were both set to zero (i.e assuming idealised blackbody conditions) (Mayer et al., 2025).

Normally, atmospheric path radiances depend on the sensor viewing geometry, including the viewing zenith angle (θ) and the viewing azimuth angle (ϕ). However, because Landsat 8 observes the surface at a near-nadir geometry ($\theta \approx 0$), the sensor receives radiance almost directly along the surface normal (i.e straight up). Thus, at nadir, path radiance is effectively independent of the viewing azimuth angle, meaning *libRadtran* can be run with $\phi = 0$ across the entire scene with negligible loss of physical accuracy (Schott et al., 2012).

The output of this process was an estimation of both upwelling and downwelling path radiances per nanometer of wavelength for each scene. Because *libRadtran* does not emulate the spectral response characteristics of the TIRS instrument, these radiance outputs were convolved with the Landsat 8 spectral response functions provided by USGS, thereby obtaining band-specific atmospheric radiance components (Yu et al., 2014).

Transmissivity (τ)

Qin et al (2001) and Yu et al (2014) demonstrated that transmissivity for Landsat bands 10 and 11 can be estimated from atmospheric water content (w). For a midlatitude summer, these relationships are essentially polynomial and depend on the water content range (see Table 2). The high R^2 and low RMSE of these relationships indicates the high degree of accuracy.

Water Content Range $[gcm^{-2}]$	Relationship of τ and w	R^2	RMSE
0.2 − 3.0	$\tau_{10} = -0.0164w^2 - 0.04203w + 0.9715$	0.9993	0.002
	$\tau_{11} = -0.01218w^2 - 0.07735w + 0.9603$	0.9996	0.002
3.0 − 6.0	$\tau_{10} = -0.00168w^2 - 0.1329w + 1.127$	0.9999	0.001
	$\tau_{11} = -0.09186w^2 - 0.2137w + 1.181$	0.9997	0.002

Table 6: Relationship of atmospheric water content to specific humidity for specific Landsat 8 bands, as per Yu et al (2013)

The ERA5 atmospheric data includes specific humidity (q) and pressure (p) which can be used to calculate precipitable water (PW) $[kgm^{-2}]$ and, in turn, water content $[gcm^{-2}]$. As shown in equation [15], PW is obtain by integrating specific humidity with respect to pressure from the bottom of the atmosphere to the top, thereby representing the total vertical column of water vapour in the atmosphere per unit of surface area:

$$PW = \frac{1}{g}\int_0^\infty q\,dp \qquad [15].$$

Where g is the gravitational constant at 6.6743e-11 $[m^3kg^{-1}s^{-2}]$.

Unlike the path radiance components, it was not necessary to weight the outputted transmissivity values by the spectral response functions of bands 10 and 11, since the equations in Table 2 are already specific to the bands. The output was a transmissivity raster at the spatial resolution of ERA5 profiles, which was then resampled to 10m using nearest-neighbour interpolation.

LST Derivation

From this point, per-scene LST was derived for both daytime and nighttime scenes by supplying the required parameters to equation [3]. Although these estimates represent the same physical quantity, they are pseudo-invariant because the scenes were captured at different times throughout Sydney's 2019−2020 summer (Cai et al., 2021). To composite these data and analyse the broader spatial structure of the UHI during the heatwave period, it was therefore necessary to normalise the LST layers using median image subtraction. This approach was selected for its robustness to outliers compared to mean-based normalisation (He et al., 2015). This is particularly important for nighttime scenes, which are more susceptible to artefacts due to their relative scarcity and the difficulty of quality masking. Following normalisation, the scenes were composited into seasonal median LST mosaics for both daytime and nighttime conditions across the study period (see Figures 2 and 3 in *Results*).

UHI and Hotspot Analysis

Since normalisation preserves relative differences, including the urban-rural contrast, UHI intensity (UHII) remains numerically unchanged (Jia et al., 2024). The UHII of a pixel i can be calculated as the difference between the pixel's LST and the rural LST mean according to equation [16]:

$$UHII_i = LST_i - LST_{rural}$$

[16].

Urban and rural pixels were delineated using the Australian Bureau of Statistics' Urban Centres and Localities dataset, which identifies areas of concentrated urban development at the Statistical Area Level 1 (SA1). This classification was applied to both daytime and nighttime composites, producing seasonal median UHII maps for Sydney's 2019-2020 summer (see Figures 4 and 5 in *Results*). A hotspot analysis was then conducted using Getis-Ord Gi*. This local spatial autocorrelation technique detects statistically significant concentrations of high or low UHII values, thereby illustrating where thermal anomalies form persistent hotspots or cool pockets within the region (ESRI, 2023). The hotspot analysis was conducted at 90m spatial resolution due to computational limitations. Finally, the analysis focussed on the distribution of UHII over different Local Climate Zones.

Validation

The modelled LST outputs were validated against the official LST product contained in the USGS Landsat Level-2 suite. Overall performance was within the expected range, with a global RMSE of 6.924 K and global MAE of 6.522 K. Performance varied across individual scenes, with per-scene RMSE values ranging from 4.075 K − 8.848 K, and MAE values ranging from 4.004 K − 8.501K. The similarity between RMSE and MAE indicates that the errors are largely systematic rather than driven by a small number of outliers, since MAE is less sensitive to extreme values (Kouzehgar & Eslamian, 2023). On the whole, the model typically produced hotter values than the USGS product. The per-scene variability is of particular note. A post-analysis revealed that the outputs with higher RMSE and MAE, were those with wet, humid conditions

with high water content and thus also low transmittance (~0.4 – 0.6). Figure … illustrates the validation pairs with lowest and highest RMSE and MAE values.
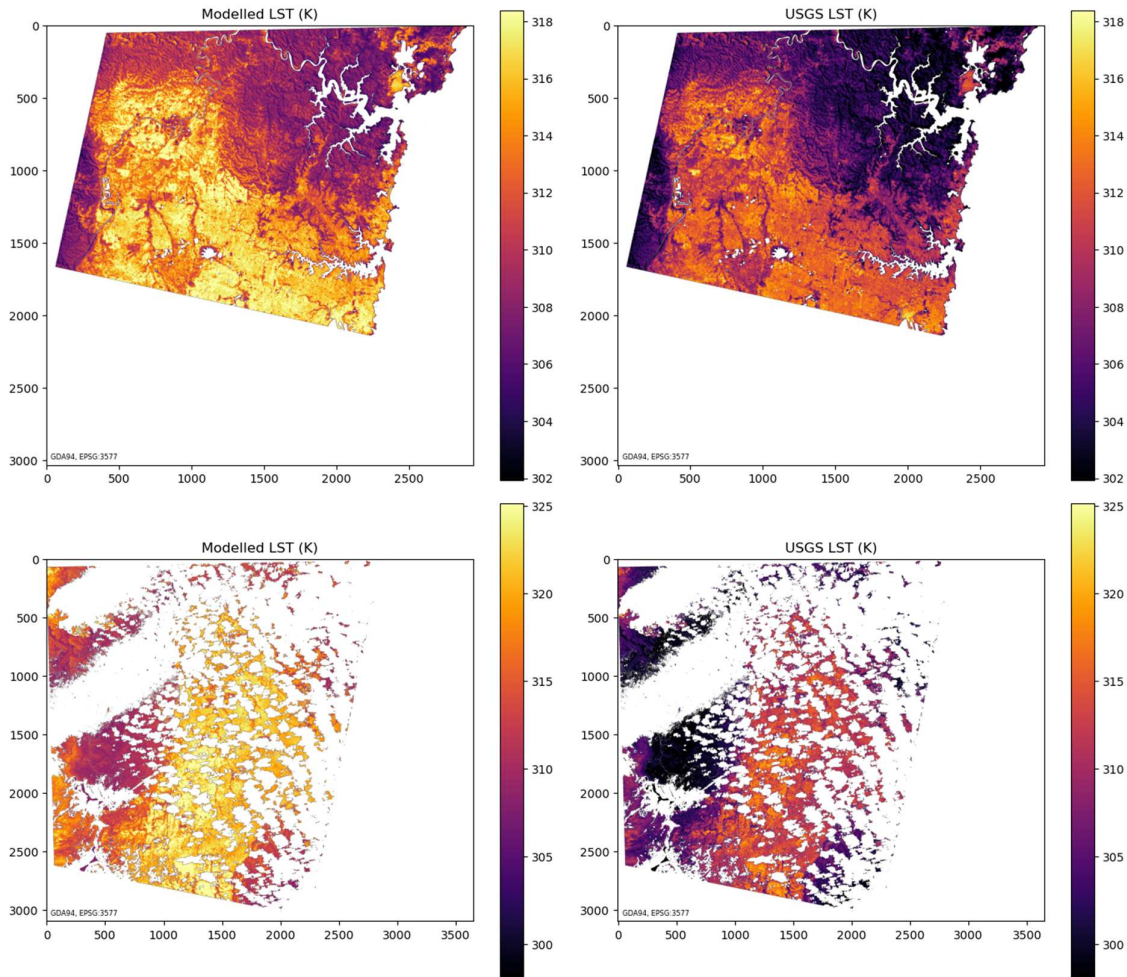

Figure 2: Two sets of validation pairs illustrating differences in model accuracy per atmospheric conditions. Top: a comparison of modelled LSTs and USGS LSTs for a dry, clear scene with high transmissivity; RMSE = 4.075. Bottom: a comparison of modelled LSTs and USGS LSTs for a humid scene with high cloud cover and low transmissivity; RMSE = 8.848.

Instability in LST inversion due to transmissivity derivation is a well-documented issue. The issue arises in the inverted LST equation [3] from the primary amplification term:

$$\frac{1}{\tau_i \varepsilon_i}$$

As transmissivity decreases, this term increases inversely and non-linearly. Consequently, even small underestimations of transmittance become strongly amplified within the inversion, dramatically increasing the sensitivity of the retrieved temperature to errors at low transmissivity (Li et al., 2013).

It is important to emphasise that this validation carries substantial uncertainty for several reasons. Firstly, no in-situ surface temperature measurements were available for the study period. As a result, the USGS Level-2 LST product was used as the reference. However, this data is itself a modelled product, and therefore embeds its own assumptions, parameterisations and biases. For instance, the USGS methodology derives emissivity exclusively through NDVI-based thresholds, a technique that has historically performed poorly in heterogeneous urban environments which undermine the NDVI-emissivity relationship (Hulley et al., 2015; Oliveira et al., 2022). Additionally, USGS performs atmospheric modelling using MODTRAN and NCEP reanalysis data (Laraby, 2017). Thus, the two models differ in their emissivity schemes and transmittance parameterisation. Errors inherent to each algorithm therefore compound when the two are compared.

Disagreement between the modelled LST and the USGS LST does not necessarily indicated that the model in this study is deficient. Published evaluations show that USGS LST typically carries uncertainties of approximately 3, with a known tendency to underestimate true surface temperatures (Duan et al., 2021). Because of this, the fact that the modelled LSTs are 4-9 K warmer than the USGS product does not necessarily imply that the model overestimates true LSTs to a greater degree. In some cases, it is possible that part of this positive bias relative to USGS reflects compensation for the known cold bias in the reference product. However, without independent in-situ data, it cannot be determined whether the model is systematically closer to true LST or not.

Results

Figure 3 represents the spatial distribution of emissivity across the Sydney region.
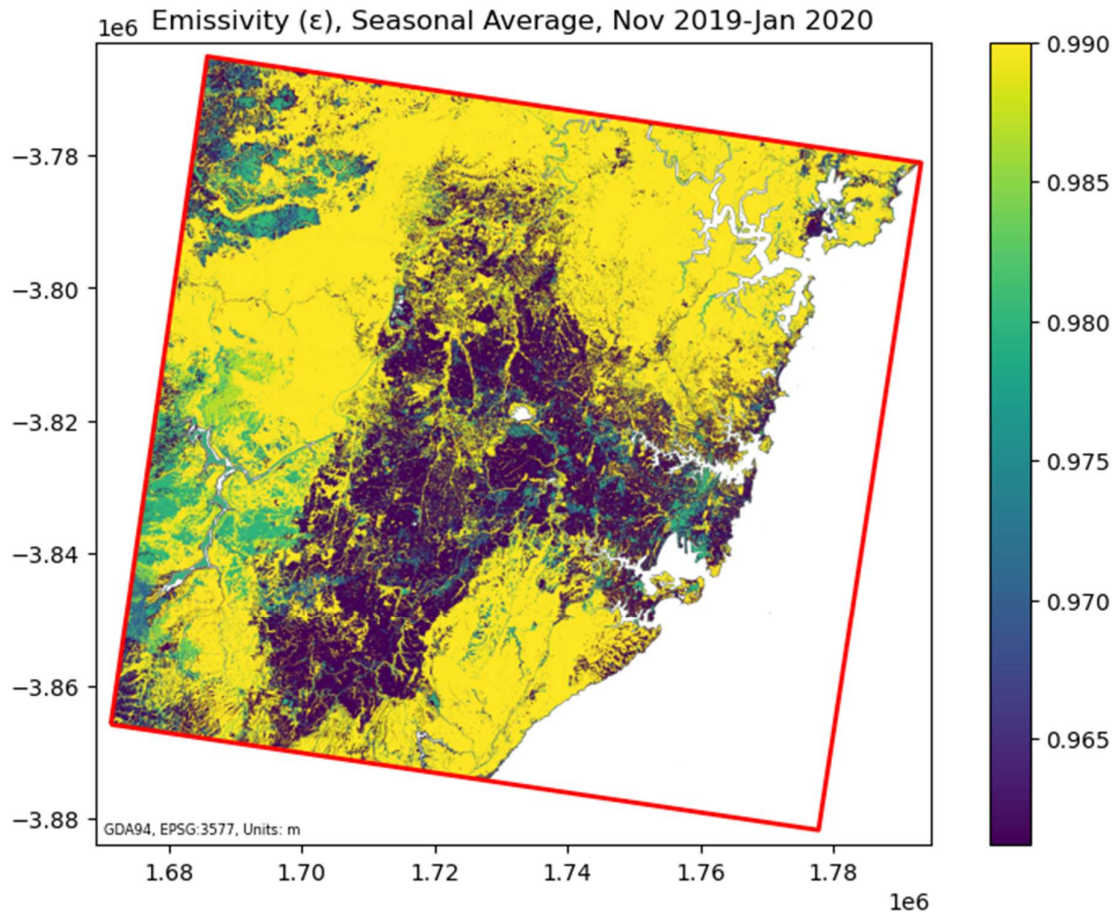
Figure 3: Pixel-wise emissivity for Sydney over the summer study period (Nov 2019 - Jan 2020).

This pixel-wise emissivity map provided an essential input for LST derivation in both day and night scenes, under the assumption that surface features, and therefore emissivity, remained relatively stable across the diurnal cycle (Oliveira et al., 2022). Figures 4 and 5 present the seasonal median UHII for daytime and nighttime conditions, respectively.
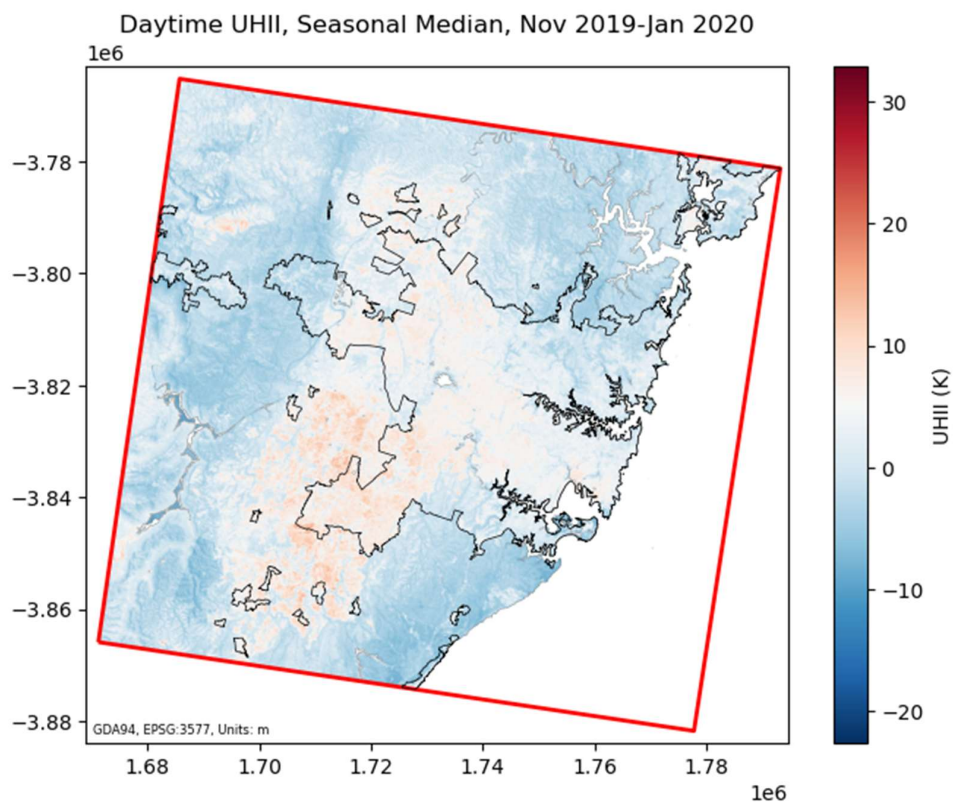
Figure 4: The seasonal UHII for Sydney's daytime after LST aggregation and normalisation. The black footprint shows urban areas as per ABS' UCL dataset. Outliers excluded for visualisation.
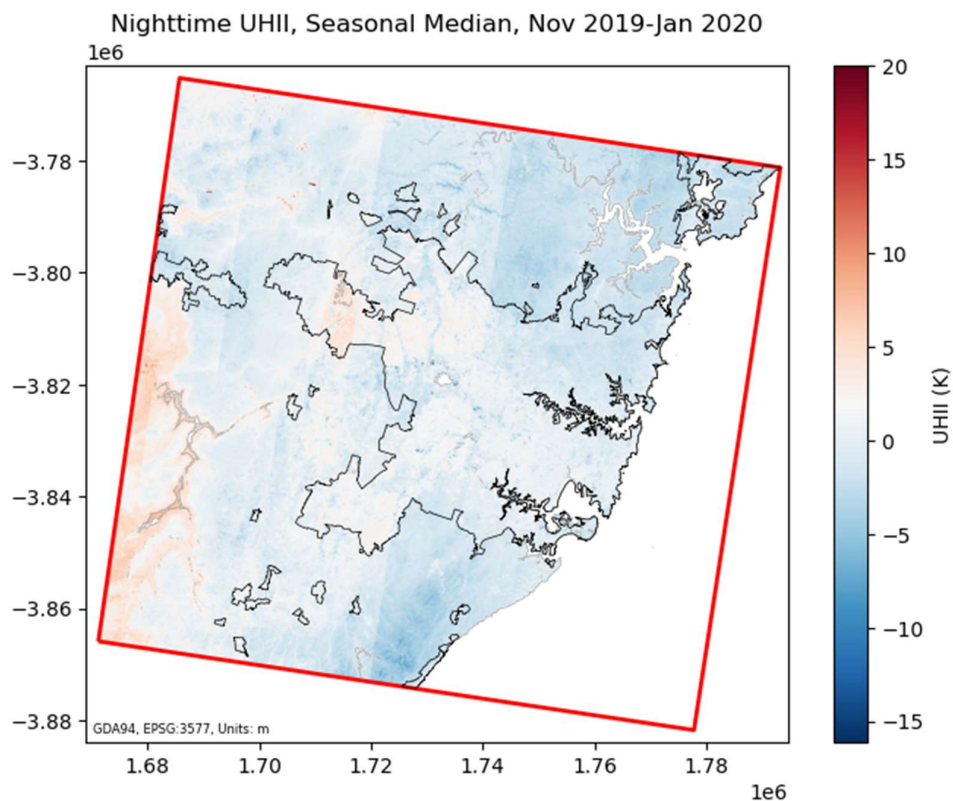

Figure 5: The seasonal UHII for Sydney's nighttime after LST aggregation and normalisation. The black footprint shows urban areas as per ABS' UCL dataset. Outliers excluded for visualisation.

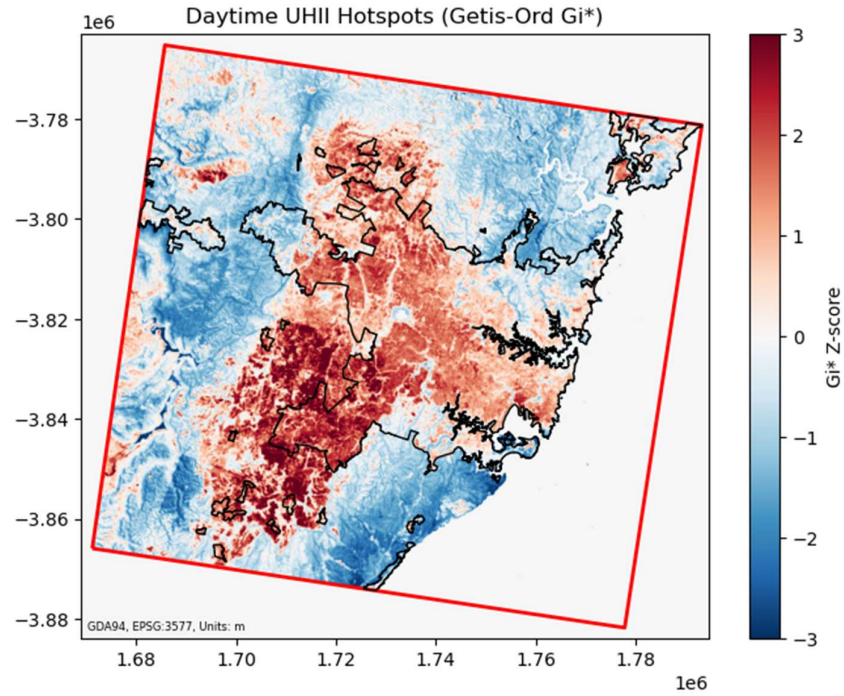The results from the Getis-Ord G* hotspot analysis are provided below in Figures 6 and 7.

Figure 6: Results from the Getis-Ord Gi hotspot analysis for seasonal daytime UHII. The black footprint shows urban areas according to ABS' UCL dataset*
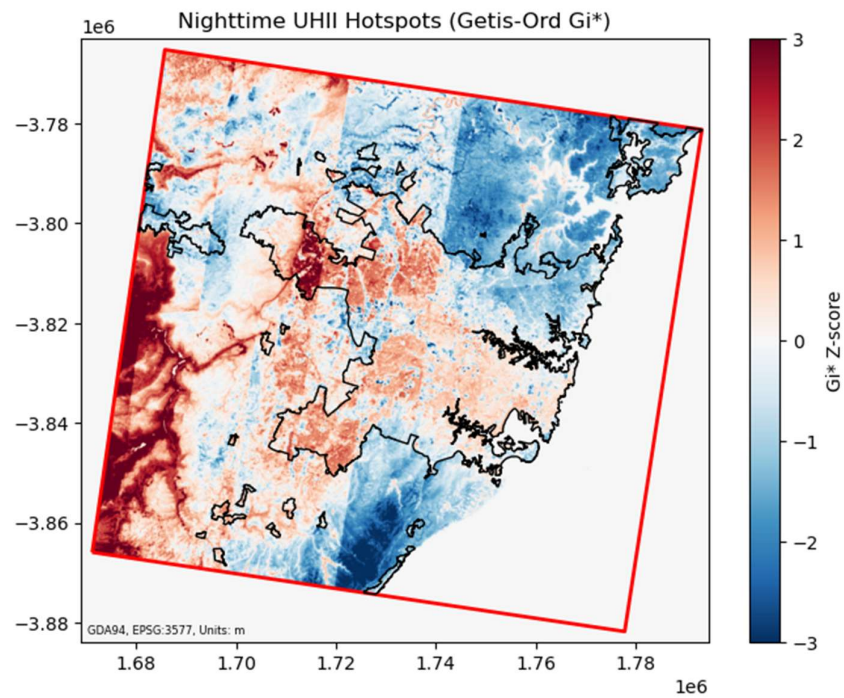

Figure 7: Results from the Getis-Ord Gi hotspot analysis for seasonal nighttime UHII. The black footprint shows urban areas according to ABS' UCL dataset.*

Finally, Figures 8 and 9 are boxplots showing the distribution of UHII across different local climate zones according to the LCZ map.
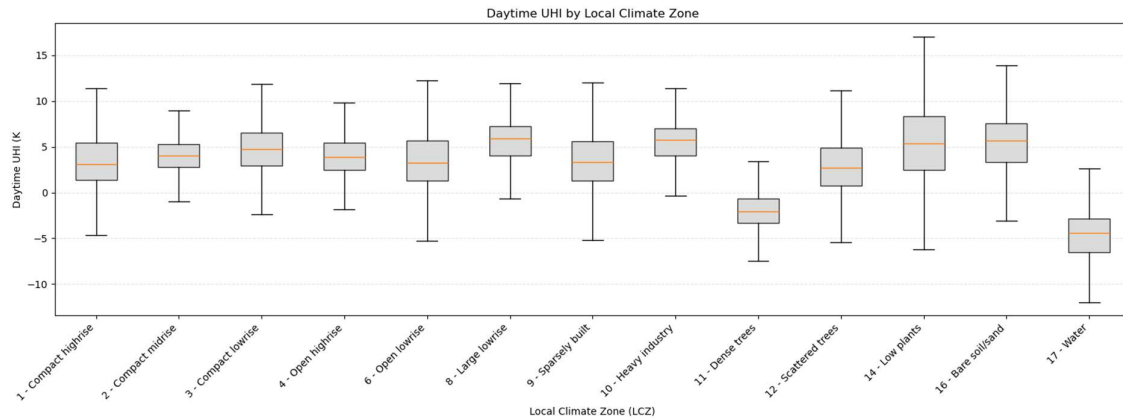

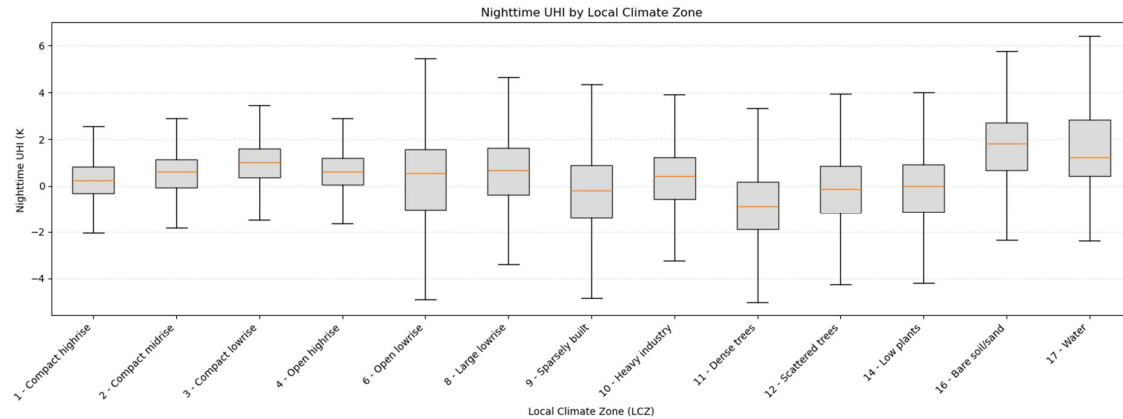*Figure 8: Boxplot showing the distribution of daytime UHII across LCZ classes.*

Figure 9: Boxplot showing the distribution of nighttime UHII across LCZ classes.

Discussion

Daytime UHII

A clear dichotomy is evident. Urban surfaces exhibit lower emissivity values, shown in purple, while vegetated areas exhibit higher emissivity, represented by yellow-green (Figure). This contrast reflects the different thermal and material properties of built-up areas versus vegetated land covers. The daytime UHII map reveals a broad, spatially-extensive warm anomaly across the inland urban portions of the study area. While many UHII values are moderate (approximately 1 to 5 K), several distinct warm pockets exceed 10 K, aligning closely with dense urban fabric, industrial zones, and low-vegetation LCZ classes, shown in Figure 6. In contrast, forested LCZs exhibit

consistently low UHII, demonstrating the strong cooling influence of dense vegetation. Scattered tree and bare-soil classes, which display higher UHII values more comparable to urban areas, further underscore the importance of vegetation cover in moderating LST (Tian et al., 2019). Along the coastline, non-urban areas often display pronounced cool pockets, with UHII values between -5 and -15 K. These patterns likely reflect the influence of coastal airflow and advective cooling processes. The daytime Getis-Ord Gi* patterns reinforce these interpretations. Large, coherent clusters of statistically significant hotspots occupy the central and western urbanised regions, whereas strong coldspots dominate densely vegetated western areas and non-urban coastal zones in the north and south. Although the hotspot layer mirrors the UHII surface, the Gi* map clarifies the spatial structure, highlighting where elevated UHII is not only present but also spatially clustered and statistically meaningful (ESRI, 2023).

Nighttime UHII

By contrast, nighttime UHII is substantially weaker across the study area. Most values fall between -5 and 5 K, and the landscape becomes more thermally uniform after sunset. This is reflected in the narrower nighttime distribution (SD = 1.95). A notable exception is the western edge of the map around Lake Burragorang, where elevated UHII persists. It is important to emphasise that the Getis-Ord Gi* statistic does not map absolute UHII intensity, but rather the spatial clustering of unusually high or low values relative to local neighbours. Around Lake Burragorang, the steep terrain likely enhances local contrasts in nighttime temperature: warmer ridges tops juxtaposed with cold-air drainage in valley floors can generate strong local anomalies that the Gi* method highlights as clusters (Steigerwald et al., 2022). Even so, the persistence of relatively strong UHII signals in this area is somewhat unexpected, as it diverges from the typical nighttime behaviour of urban heat patterns. These anomalies may therefore reflect methodological limitations or artefacts, as discussed later under *Limitations and Assumptions*.

LCZs

Overall, daytime UHII patterns show large class separation with strong contrasts. Urban LCZs (1 - 10) show consistently positive UHII, typically centred between 3 – 7 K above the rural reference, with upper extremes exceeding 10 – 12 K in several zones. The heavy industry LCZ displays the highest daytime median, reflecting the reduced cooling effects of dense built forms, impervious surfaces, and reduced vegetation. Vegetated LCZs, particularly dense trees (LCZ 11), act as prominent daytime cool zones, often with UHII values below the rural reference. Bare soil/sand (LCZ 16) and low plants (LCZ 14) show surprisingly warm daytime medians, at times overlapping with urban LCZs perhaps underscoring the thermal sensitivity of exposed soils. At night, the UHII distribution compresses substantially. Most LCZs cluster around UHII values between -1 and 2 K, indicating a more uniform thermal landscape. Urban LCZs still tend to remain slightly warmer than surrounding landscapes, but the separation between classes is far smaller than during the day. From day to night, urban LCZs exhibit slightly lower UHII values relative to the rural reference compared with their daytime behaviour. In contrast, bare soil/sand and low-plant LCZs show the largest day-night differences, reflecting the rapid nocturnal cooling of natural surfaces with low thermal inertia.

Drivers of UHII Variability

Overall, the observed patterns are highly consistent with established urban heat island theory. The results highlight the fundamental diurnal asymmetry between urban and natural surfaces, reflecting the strong influence of surface structure, material properties, and vegetation cover on thermal behaviour (Christen et al., 2017). Industrial zones (LCZ 10), characterised by metal roofing, concrete hardstand and minimal vegetation, exhibit high thermal inertia and therefore behave similarly to compact urban classes. High impervious fractions within built LCZs promote strong daytime heating due to their low albedo, high thermal admittance, and substantial capacity for heat storage (Chrysoulakis et al., 2018). In compact urban forms (LCZ 1-3), canyon geometry further amplifies heating by trapping and repeatedly reflecting shortwave radiation, increasing the net absorbed energy (Khalvandi & Karimimoshaver, 2025).

In contrast, sparse-vegetation LCZs heat rapidly during the day because limited canopy cover reduces evapotranspiration, thereby removing a major cooling mechanism during peak insolation and allowing exposed soils and bare surfaces to warm efficiently (Tian et al., 2019). Vegetated LCZs, however, remain relatively cool both during the day and at night because they store little heat, maintain higher emissivity, and facilitate evapotranspiration (Guillevic et al., 2003). Finally, although all LCZs cool after sunset, built-up areas retain heat for longer due to high thermal inertia, whereas natural areas cool more rapidly.

Limitations and Assumptions

Several limitations can be identified which may contribute to error. Multiple assumptions underpin the atmospheric modelling used in this study. The atmospheric profiles supplied to *libRadtran* contain only a vertical dimension and lack any latitude-longitude structure. This enforces the assumption of a plane-parallel atmosphere, whereby atmospheric gases and aerosols are treated as horizontally homogeneous. Because transmittance and radiance are strongly influenced by horizontal variability, especially in water vapour, this simplification necessarily overlooks important spatial heterogeneity. As a consequence, *libRadtran* produces a single atmospheric solution (i.e one set of upwelling and downwelling radiance) per scene, rather than spatially varying estimates. Over large or atmospherically diverse areas, this assumption can introduce uncertainty into the model or otherwise break down under the earth's curvature (Wang, 2017). The assumption of a plane-parallel atmosphere is reasonable in this case. The study area was relatively small, and heatwaves typically represent synoptically stable conditions, in which pressure gradients of gasses slacken horizontally and there are no strong mixing events (Oliveira et al., 2022).

Another assumption embedded in *libRadtran* is that surfaces behave as Lambertian emitters, meaning that they radiate uniformly in all directions. Real surfaces, however, are not perfectly Lambertian. Many materials, such as those found in urban surfaces, exhibit ansiotropicity where emission varies with viewing angle. This angular dependence can lead to mismatches between modelled radiance and the radiance actually captured by TIRS, especially when the sensor observes at an

oblique geometry rather than being strictly nadir. Consequently, the Lambertian assumption can introduce additional bias into LST retrievals when real surfaces do not behave in an ideal way (Mayer et al., 2025).

Finally, data availability was extremely lacking. Patchy availability of nighttime scenes heightens uncertainty for aggregation, especially when the data is from a variety of temporal and atmospheric contexts. Indeed, seams are evident in the aggregated nighttime figures, despite normalisation. Additionally, the trade-off of normalisation is that, while it preserves the spatial pattern of LST and enables multitemporal aggregation and mosaicking, it removes absolute temperature information and thus precludes direct inter-scene comparisons of LST (Cai et al., 2021).

This is an issue that cannot be easily overcome given the rarity of Landsat nighttime scenes. However, it provides an avenue for further research for using machine learning to estimate nighttime LSTs, by training a ML model on nighttime data that has been connected spatiotemporally to the daytime data. Such ML models could be used on daytime scenes, where there are no connected nighttime scenes, to estimate a Landsat-like LST surface. Oliveira et al (2022) demonstrates the effectiveness of such modelling, especially when it considers how various components of the energy budget are partitioned.

Conclusion

This study successfully retrieved daytime and nighttime LSTs from Landsat 8/9 Level-1 data and applied these to quantify the UHII across Greater Sydney. By applying a full radiative-transfer workflow, this study generated high-resolution daytime and nighttime UHII maps for Sydney during the 2019−2020 summer. Integration with ABS UCL data enabled urban-rural comparisons, while LCZ classifications showed how urban morphology mediates both daytime heating and nocturnal cooling. Overall, this project demonstrates the utility of combining Landsat thermal data, ERA5 reanalysis profiles, and urban form datasets to characterise UHI behaviour at fine spatial scales. Comparisons with the USGS LST product demonstrated average agreement, despite inherent differences in emissivity schemes and atmospheric modelling. Further validation is yet required.

Code Availability

The complete workflow and code is available at:
https://github.com/DreadZone11/GEOM7001-LST-UHII

GenAI Statement

ChaptGPT was used for outlining and proofreading. No new content was AI-generated, including text, images or diagrams.

Bibliography

Australian Bureau of Statistics. (2021). *Urban Centres and Localities* (No.

1270.0.55.004) [Dataset].

C3S. (2018). *ERA5 hourly data on single levels from 1940 to present* [Dataset].

Copernicus Climate Change Service (C3S) Climate Data Store (CDS).

https://doi.org/10.24381/CDS.ADBB2D47

Cai, Z., Fan, C., Chen, F., & Li, X. (2021). Pseudo-Invariant Feature-Based Linear

Regression Model (PIF-LRM): An Effective Normalization Method to Evaluate

Urbanization Impacts on Land Surface Temperature Changes. *Atmosphere*,

12(11), 1540. https://doi.org/10.3390/atmos12111540

Candra, D. S., Phinn, S., & Scarth, P. (2019). Automated Cloud and Cloud-Shadow

Masking for Landsat 8 Using Multitemporal Images in a Variety of

Environments. *Remote Sensing*, *11*(17), 2060.

https://doi.org/10.3390/rs11172060

Chavez, J., Pat. (1996). Image-Based Atmospheric Corrections—Revisited and

 Improved. *Photogrammetric Engineering and Remote Sensing*, *62*, 1025–1036.

Chavez, P. S. (2014). *Re: What is the correct procedure for dark object subtraction?*

 [Post]. Researchgate.

 https://www.researchgate.net/post/What_is_the_correct_procedure_for_dark

 _object_subtraction

Christen, A., Mills, G., Voogt, J. A., & Oke, T. R. (Eds.). (2017). Urban Heat Island. In

 Urban Climates (pp. 197–237). Cambridge University Press.

 https://doi.org/10.1017/9781139016476.008

Chrysoulakis, N., Grimmond, S., Feigenwinter, C., Lindberg, F., Gastellu-Etchegorry, J.-

 P., Marconcini, M., Mitraka, Z., Stagakis, S., Crawford, B., Olofson, F., Landier,

 L., Morrison, W., & Parlow, E. (2018). Urban energy exchanges monitoring

 from space. *Scientific Reports*, *8*(1), 11498. https://doi.org/10.1038/s41598-

 018-29873-x

Demuzere, M., Kittner, J., Martilli, A., Mills, G., Moede, C., Stewart, I. D., van Vliet, J., &

 Bechtel, B. (2022). A global map of local climate zones to support earth

 system modelling and urban-scale environmental science. *Earth System

 Science Data*, *14*(8), 3835–3873. https://doi.org/10.5194/essd-14-3835-2022

Duan, S.-B., Li, Z.-L., Zhao, W., Wu, P., Huang, C., Han, X.-J., Gao, M., Leng, P., & Shang,

 G. (2021). Validation of Landsat land surface temperature product in the

 conterminous United States using in situ measurements from SURFRAD,

ARM, and NDBC sites. *International Journal of Digital Earth*, *14*(5), 640–660.

https://doi.org/10.1080/17538947.2020.1862319

ESRI. (2023). *Hot Spot Analysis (Getis-Ord Gi*)*. ESRI. https://pro.arcgis.com/en/pro-

app/latest/tool-reference/spatial-statistics/hot-spot-analysis.htm

Guillevic, P., Gastellu-Etchegorry, J. P., Demarty, J., & Prévot, L. (2003). Thermal

infrared radiative transfer within three-dimensional vegetation covers.

Journal of Geophysical Research: Atmospheres, *108*(D8).

https://doi.org/10.1029/2002JD002247

He, K., Zhang, X., Ren, S., & Sun, J. (2015). Deep residual learning for image

recognition. *arXiv*, *1512.03385*.

Hulley, G., Hook, S., Abbot, E., Malakar, T., & Islam, M. (2015). *The ASTER Global

Emissivity Database (ASTER GED): Mapping Earth's emissivity at 100 meter

spatial resolution*. NASA.

https://lpdaac.usgs.gov/documents/121/ASTERGED_User_Guide_V4.pdf?ut

m_source=chatgpt.com

Jia, R., Liu, J., He, T., Han, D., Xu, X., Liu, L., Sun, Z., & Qiao, Z. (2024). Population heat

exposure risk from the perspective of urban heat island spatial expansion in

China during 2005–2020. *Urban Climate*, *56*, 101987.

https://doi.org/10.1016/j.uclim.2024.101987

Khalvandi, R., & Karimimoshaver, M. (2025). Urban street canyons and heat islands:

A systematic review on morphological solutions. *Results in Engineering*, *27*,

106542. https://doi.org/10.1016/j.rineng.2025.106542

Kouzehgar, K., & Eslamian, S. (2023). Application of experimental data and soft computing techniques in determining the outflow and breach characteristics in embankments and landslide dams. In *Handbook of Hydroinformatics* (pp. 11–31). Elsevier. https://doi.org/10.1016/B978-0-12-821962-1.00002-7

Laraby, K. (2017). Landsat Surface Temperature Product: Global Validation and Uncertainty Estimation. *RIT Scholar Works*.

Li, Z.-L., Tang, B.-H., Wu, H., Ren, H., Yan, G., Wan, Z., Trigo, I. F., & Sobrino, J. A. (2013). Satellite-derived land surface temperature: Current status and perspectives. *Remote Sensing of Environment*, *131*, 14–37. https://doi.org/10.1016/j.rse.2012.12.008

Mao, Q., Peng, J., & Wang, Y. (2021). Resolution Enhancement of Remotely Sensed Land Surface Temperature: Current Status and Perspectives. *Remote Sensing*, *13*(7), 1306. https://doi.org/10.3390/rs13071306

Mayer, B., Kylling, A., Emde, C., Hamann, U., Buras, R., Gasteiger, J., Jakub, F., & Richter, B. (2025). *libRadtran User's Guide*.

Muller, C. L., Chapman, L., Grimmond, C. S. B., Young, D. T., & Cai, X. (2013). Sensors and the city: A review of urban meteorological networks. *International Journal of Climatology*, *33*(7), 1585–1600. https://doi.org/10.1002/joc.3678

Oke, T. R. (1982). The energetic basis of the urban heat island. *Quarterly Journal of the Royal Meteorological Society*, *108*(455), 1–24. https://doi.org/10.1002/qj.49710845502

Oliveira, A., Lopes, A., Niza, S., & Soares, A. (2022). An urban energy balance-guided machine learning approach for synthetic nocturnal surface Urban Heat Island prediction: A heatwave event in Naples. *Science of The Total Environment*, *805*, 150130. https://doi.org/10.1016/j.scitotenv.2021.150130

Schott, J., Gerace, A., Brown, S., Gartley, M., Montanaro, M., & Reuter, D. C. (2012). Simulation of Image Performance Characteristics of the Landsat Data Continuity Mission (LDCM) Thermal Infrared Sensor (TIRS). *Remote Sensing*, *4*(8), 2477–2491. https://doi.org/10.3390/rs4082477

Sharifi, E., & Lehmann, S. (2014). Comparative Analysis of Surface Urban Heat Island Effect in Central Sydney. *Journal of Sustainable Development*, *7*, 23–23. https://doi.org/10.5539/jsd.v7n3p23

Steigerwald, F., Kossmann, M., Schau-Noppel, H., Buchholz, S., & Panferov, O. (2022). Delimitation of Urban Hot Spots and Rural Cold Air Formation Areas for Nocturnal Ventilation Studies Using Urban Climate Simulations. *Land*, *11*(8), 1330. https://doi.org/10.3390/land11081330

Tian, J., Song, S., & He, H. (2019). The relationship between soil emissivity and soil reflectance under the effects of soil water content. *Physics and Chemistry of the Earth, Parts A/B/C*, *110*, 133–137. https://doi.org/10.1016/j.pce.2018.11.006

Wang, B. (2017). A Unified Formulation of Radiative Transfer in Plane-Parallel Atmospheres Based on General Decomposition of Radiance. Part II: An Exemplifying Application to the Hemispherical Harmonics Method with Four

Components. *Journal of the Atmospheric Sciences*, *74*(12), 4153–4176.

https://doi.org/10.1175/JAS-D-17-0024.1

Wicki, A., & Parlow, E. (2017). Multiple Regression Analysis for Unmixing of Surface

Temperature Data in an Urban Environment. *Remote Sensing*, *9*(7), 684.

https://doi.org/10.3390/rs9070684

Yu, X., Guo, X., & Wu, Z. (2014). Land Surface Temperature Retrieval from Landsat 8

TIRS—Comparison between Radiative Transfer Equation-Based Method, Split

Window Algorithm and Single Channel Method. *Remote Sensing*, *6*(10), 9829–

9852. https://doi.org/10.3390/rs6109829

Yun, G. Y., Ngarambe, J., Duhirwe, P. N., Ulpiani, G., Paolini, R., Haddad, S.,

Vasilakopoulou, K., & Santamouris, M. (2020). Predicting the magnitude and

the characteristics of the urban heat island in coastal cities in the proximity

of desert landforms. The case of Sydney. *Science of The Total Environment*,

709, 136068. https://doi.org/10.1016/j.scitotenv.2019.136068

Zanter, K. (2016). Landsat 8 (L8) Data User's Handbook. *USGS Official Website*, *33*.